



Synthesis of Zeolite-Supported Magnesia/Magnetite Nanoparticles, and its Efficient Application in Ultrasound-Assisted Adsorption of Dairy Wastewater: Optimization and Modeling of the Process by RSM and ANN

Ali Mehrizad*^{ID}

Department of Chemistry, Tabriz Branch, Islamic Azad University, Tabriz, Iran

Abstract

Background & Aims: Dairy industries are among the major sectors consuming huge amounts of water converting it into effluents during various processes. Developing an efficient method to treat such effluents is inevitable. In this research, *magnesium oxide* iron oxide (MgO-Fe₃O₄)-zeolite was used in the ultrasound-assisted adsorption of dairy wastewater.

Materials and Methods: The MgO-Fe₃O₄-zeolite composite was prepared via a facile method. Batch adsorption experiments were conducted on a laboratory scale. Typically, 200 mL of the effluent was poured into an Erlenmeyer flask and sonicated in the presence of an adsorbent. The effects of four factors (i.e., initial chemical oxygen demand [COD], adsorbent dosage, pH, and time) at five different levels were surveyed and optimized by response surface methodology (RSM) and artificial neural network (ANN). Finally, the analysis of variance was performed to assess the accuracy and validity of the models.

Results: Using RSM, the optimization of the adsorption process led to a swift reduction in COD (83.22%) within 20 minutes at an initial COD of 300 mgL⁻¹, an adsorbent dosage of 4 gL⁻¹, and a pH of 9. The modeling of the process by the ANN demonstrated that the adsorbent dosage was the most important factor with a 38.30% impact on the COD extent. The isothermal and kinetics studies indicated that the process could be attributed to chemical adsorption. Studies associated with thermodynamics revealed that this process was endothermic and spontaneous.

Conclusion: Based on the findings, it is concluded that the MgO-Fe₃O₄-zeolite has considerable potential in reducing the COD of dairy wastewater as a magnetically separable adsorbent.

Keywords: Adsorption, Waste water, Zeolite, MgO-Fe₃O₄, RSM, ANN

Received: June 3, 2021, Accepted: November 7, 2021, ePublished: September 29, 2022

1. Introduction

Industrial waste management is one of the significant challenges in making the balance between industry and the environment. Dairy industry wastewater with high organics is considered as one of the most polluting kinds of wastewater. It is mainly caused by washing tanks, pipes, and facilities. Approximately 0.5%-5% of input raw milk is detected in the effluent of the dairy industry, making the chemical and biochemical oxygen demand (COD and BOD) of dairy wastewater extremely high. On the other hand, such effluents would stink in a short time and cause an intense odor [1,2]. The conventional treatments for dairy wastewater mainly include physical (flotation, flocculation, and coagulation) and biological (aerobic and anaerobic) methods which are time-consuming and costly [3]. Considering that the main goal of dairy effluent treatment is to remove organic compounds, alternative treatment techniques (e.g., adsorption) could be taken into account. Adsorption is still a promising method owing to its effortless implementation, low operating costs, and the fact that it does not need sophisticated

equipment [4-6].

The selection of a suitable and efficient adsorbent is the infrastructure of adsorption processes. Traditionally, zeolite as an adsorbent has always been considered because of its individual properties such as a high surface area and a large number of cavities. Even today, zeolite-based adsorbents have extensive applications [7-9]. Magnesia (magnesium oxide, MgO) has also been utilized as an adsorbent thanks to its unique properties such as facile synthesis, environmental compatibility, accessibility, and non-toxicity [10-12].

Zeolite-based magnesia compounds are among the most popular adsorbents that, by a synergistic effect, could overcome most problems triggered by the removal of organic and inorganic pollutants in liquid or gaseous phases [13-15].

Despite all the above-mentioned descriptions, the separation of the used adsorbent is the weakness of all the adsorbents, including the magnesia-zeolite composition. The most prevalent methods include filtration and precipitation, which are always problematic, since



adsorbent particles may block the filter or pass through it. Moreover, secondary pollution may occur by the released adsorbents. In recent years, the magnetic separation process has been presented as an alternative method for overcoming these problems and facilitating the separation and recovery of the adsorbents [16,17]. In this regard, magnetite (iron oxide, Fe_3O_4) has been widely used due to its facile synthesis, low cost, physicochemical stability, and biocompatibility [18-20].

Ultrasound irradiation is able to accelerate physicochemical processes due to aquatic cavitation, thus it is expected that the adsorption process by the ultrasound-assisted method is appropriate for wastewater treatment. In fact, the cavitation phenomenon involves the formation, growth, and collapse of bubbles in the liquid phase, which can facilitate the adsorbate-adsorbent mass transfer [21,22].

The aim/novelty of this study is to synthesize and evaluate the performance of a new ternary magnesia-magnetite-zeolite composite ($\text{MgO-Fe}_3\text{O}_4$ -zeolite) as an adsorbent in the adsorption of dairy wastewater. The ternary composite was prepared, characterized, and applied as an adsorbent. To save time and cost, ultrasound-assisted adsorption experiments were designed, optimized, and modeled by response surface methodology (RSM) and artificial neural network (ANN). Eventually, adsorption isotherms, kinetics, and thermodynamics were evaluated under optimal conditions.

2. Materials and Methods

2.1. Materials

Iron (II) chloride tetrahydrate ($\text{FeCl}_2 \cdot 4\text{H}_2\text{O}$), iron (III) chloride hexahydrate ($\text{FeCl}_3 \cdot 6\text{H}_2\text{O}$), sodium hydroxide (NaOH), and magnesium nitrate hexahydrate ($\text{Mg}(\text{NO}_3)_2 \cdot 6\text{H}_2\text{O}$) were purchased from Merck Company, Darmstadt Germany. Further, zeolite type 4A ($\text{Na}_{12}[(\text{SiO}_2)_{12}(\text{AlO}_2)_{12}]27\text{H}_2\text{O}$) was obtained from Afrazand Mineral Company, Iran.

The dairy wastewater was collected from the industrial wastewater treatment plant located in Parsabad, Iran. The wastewater sample was obtained following the separation of suspended solids/fat materials from the homogenizer tank. The sample was stored at 4°C ($\text{COD}: 900 \pm 50 \text{ mg L}^{-1}$).

Distilled (DI) water was used in all experiments, and the pH of the solutions was adjusted using 0.1 M HCl or NaOH.

2.2. Adsorbent synthesis and characterization

The adsorbent synthesis was performed according to the following hierarchy:

To synthesize Fe_3O_4 , 100 mL of DI water was poured into a 3-necked round-bottomed flask, and the stoichiometric amounts of iron (II) chloride (5 mmol) and iron (III) chloride (10 mmol) were added under an N_2 atmosphere. The mixture was stirred vigorously. Once the temperature

of the mixture reached 60°C , 10 mL of sodium hydroxide (5 M) was gradually added, and the obtained mixture was stirred for another 30 minutes. After cooling the mixture, the sediments were gathered with a magnet and washed with DI water to become neutral. The obtained product was dried overnight at room temperature. Fe_3O_4 nanoparticles were obtained after crushing [23].

The magnesia-magnetite ($\text{MgO-Fe}_3\text{O}_4$) nanoparticles were prepared through a procedure that was already reported by Mahmoudi and Behnajady [24]. The stoichiometric amounts of magnesium nitrate (10 mmol) and sodium hydroxide (20 mmol) were separately dissolved in 20 mL of DI water. Thereafter, 0.2 g of Fe_3O_4 was added to the solution containing Mg^{2+} ions, and while the mixture was being heavily stirred, the aqueous solution of NaOH was added dropwise. Afterward, the sediments were centrifuged, washed with ethanol and DI water, and dried overnight at room temperature. $\text{MgO-Fe}_3\text{O}_4$ was obtained following powder calcination for 2 hours at 300°C . The pure MgO was synthesized by the use of this method without Fe_3O_4 .

To prepare $\text{MgO-Fe}_3\text{O}_4$ -zeolite, a proper amount of zeolite was dispersed in 100 mL DI water in an ultrasonic bath. Subsequently, the washed sediments from the previous step ($\text{MgO-Fe}_3\text{O}_4$) were added to the zeolite suspension, and the resulting mixture was stirred on a magnetic stirrer for 4 hours. Following centrifugation and drying at room temperature, the specimen was calcined for 2 hours at 300°C until obtaining the composite [25].

The structural, morphological, surface, and magnetic features of the synthesized powders were extensively characterized by different methods, including X-ray diffraction (XRD, X' Pert Pro, Panalytical), field emission-scanning electron microscopy (FE-SEM, ZEISS-Sigma VP), and transmission electron microscopy (TEM, ZEISS, EM10C, 100 kV). The other methods were energy dispersive X-ray spectroscopy (EDX, Oxford Instruments), vibrating sample magnetometer (VSM, Meghnatis Daghigh Kavir Co. LBKFB), and N_2 adsorption/desorption isotherms (BEISORP Mini-Microtrac Bel Corp).

2.3. Ultrasound-assisted adsorption experiments

Batch adsorption experiments were conducted on a laboratory scale. Typically, 200 mL of the dairy effluent with a specific pH and initial COD was poured into an Erlenmeyer flask and sonicated after adding an appropriate amount of the adsorbent. Sampling was performed at a given time, and the adsorbent was seceded from the solution by employing a strong magnet. The supernatant was transferred into a vial, and COD was quantified using HACH-DR/890 colorimeter equipped with the HACH-DRB 200 thermal reactor as per the instruction. The extent of the COD reduction (COD_r , %) and the adsorption capacity (mg g^{-1}) at time t (q_t)

and equilibrium (q_e) were calculated using Eqs. (1-3), respectively:

$$COD_r(\%) = \frac{(C_0 - C_t)}{C_0} \times 100 \quad (1)$$

$$q_t = \frac{(C_0 - C_t)}{m} \times V \quad (2)$$

$$q_e = \frac{(C_0 - C_e)}{m} \times V \quad (3)$$

where C_0 , C_t , and C_e are the initial, time t , and the equilibrium COD contents of the effluent (mgL^{-1}), respectively. Further, V and m denote the volume of the solution (L) and the amount of the adsorbent (g), respectively.

After performing preliminary trials and finding the major influential parameters, the effects of four factors at five different levels (Table 1) were surveyed and optimized by the central composite design (CCD) based on RSM (Design-Expert[®] 11 software). The ANN modeling was also utilized to select the important operational parameter and the reoptimization of the adsorption process. The analysis of variance (ANOVA) was performed to assess the accuracy and validity of the models. Detailed explanations of RSM and ANN are provided in our previous research work [26].

3. Results

3.1. Characterization of synthesized powders

The FE-SEM and TEM images were enacted to enlighten the morphological properties of the prepared powders (Figure 1). MgO and Fe_3O_4 spherical nanoparticles with relatively uniform sizes (Figures 1a and b), as well as 4A zeolite cubic particles (Figure 1c), were well formed based on visual observation. Furthermore, we clearly observed the widely distributed MgO aggregated with Fe_3O_4 particles (Figure 1d), along with the settled MgO- Fe_3O_4 on the porous surface of zeolite with abundant irregular protrusions (Figure 1e).

In addition, the TEM image (Figure 1f) confirmed the composite formation, in which the dark spots represented the Fe_3O_4 nanoparticles and the other components (MgO and zeolite) had light colors; the difference in the components' colors is due to their different levels of electron permeability.

Figure 2a shows the XRD patterns of the prepared powders. In the XRD pattern of MgO, five distinct peaks appeared at the diffraction angles of 36.79, 42.83, 62.14, 74.44, and 78.46°, respectively. These angles correspond to crystal planes with Miller indices (1 1 1), (2 0 0), (2 2 0), (3 1 1), and (2 2 2), which are fully matched with the peaks of the pure cubic MgO index (JCPDS card no. 45-0946) [27]. For Fe_3O_4 , the prominent peak at 35.71° belongs to a crystal plane with Miller indices (3 1 1). The other broad peaks at $2\theta = 30.31^\circ$ (2 2 0), 43.37° (4 0 0),

Table 1. Domain of the operational parameters and designed experiments, along with experimental and predicted results

Parameters	Levels				
	-2	-1	0	+1	+2
X_1 : COD_0 (mg L^{-1})	100	300	500	700	900
X_2 : Adsorbent dosage (g L^{-1})	1	2	3	4	5
X_3 : pH	3	5	7	9	11
X_4 : Time (min)	5	10	15	20	25

Std.	Coded values of parameters				Exp.	COD _r (%)	
	X_1	X_2	X_3	X_4		RSM Pred.	ANN Pred.
1	-1	-1	-1	-1	53.11	53.49	53.58
2	1	-1	-1	-1	44.83	42.57	45.13
3	-1	1	-1	-1	63.82	62.38	64.51
4	1	1	-1	-1	51.92	50.91	52.37
5	-1	-1	1	-1	61.89	63.03	62.54
6	1	-1	1	-1	50.2	50.97	50.61
7	-1	1	1	-1	74.1	75.80	75.00
8	1	1	1	-1	63.21	63.19	63.89
9	-1	-1	-1	1	66.13	65.82	66.87
10	1	-1	-1	1	56.57	55.52	57.11
11	-1	1	-1	1	68.68	68.56	69.47
12	1	1	-1	1	59.17	57.70	59.76
13	-1	-1	1	1	74.08	75.75	74.98
14	1	-1	1	1	63.2	64.31	63.88
15	-1	1	1	1	80.43	82.36	81.46
16	1	1	1	1	70.09	70.37	70.91
17	-2	0	0	0	71.26	68.95	72.10
18	2	0	0	0	44.05	46.04	44.33
19	0	-2	0	0	57.32	56.76	57.88
20	0	2	0	0	71.47	71.71	72.31
21	0	0	-2	0	45.51	49.31	45.82
22	0	0	2	0	75.64	71.51	76.57
23	0	0	0	-2	58.25	58.79	58.82
24	0	0	0	2	79.17	78.31	80.17
25	0	0	0	0	60.89	60.47	61.52
26	0	0	0	0	57.93	60.47	58.50
27	0	0	0	0	63.8	60.47	64.49
28	0	0	0	0	61.28	60.47	61.92
29	0	0	0	0	59.43	60.47	60.03
30	0	0	0	0	59.51	60.47	60.11

Note. RSM: Response surface methodology; ANN: Artificial neural network; COD: Chemical oxygen demand.

57.39° (5 1 1), and 62.86° (4 4 0), along with a noisy peak at 74.02° (4 4 4), are in an acceptable agreement with the standard magnetite diffraction pattern (JCPDS card No. 19-0629) [23]. The broad peaks suggest the formation of fine particles with low crystallinity, while sharp peaks indicate a highly crystalline structure [28]. Accordingly,

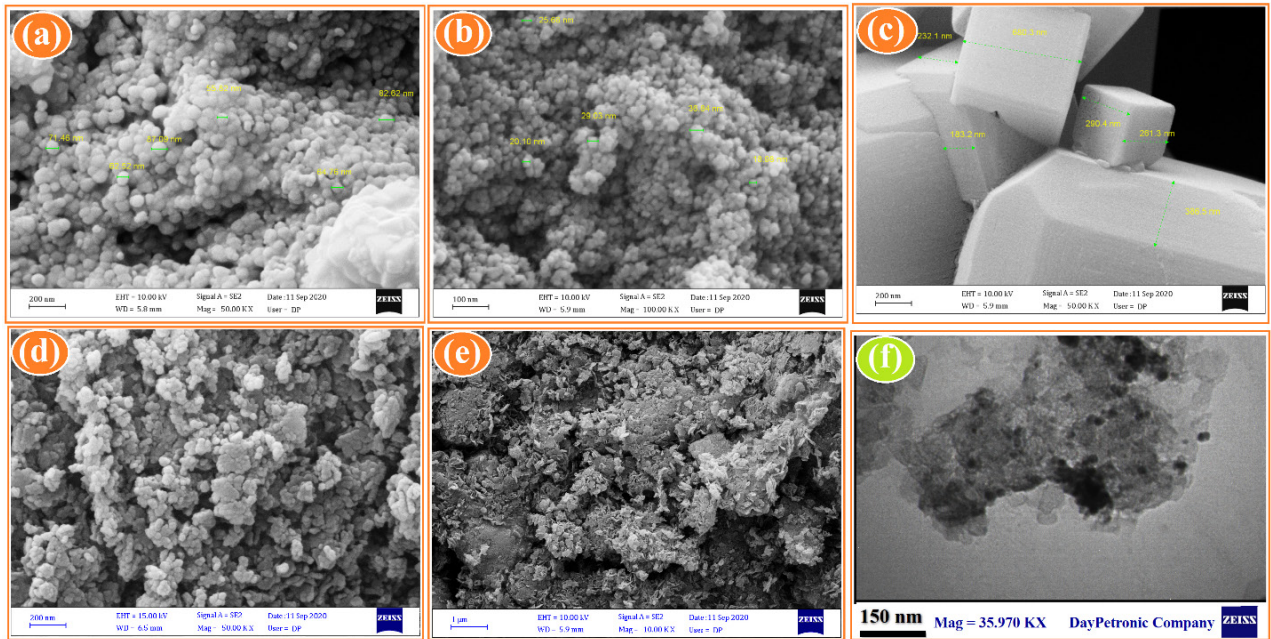


Figure 1. FE-SEM images of MgO (a), Fe₃O₄ (b), 4A-zeolite (c), MgO-Fe₃O₄ (d), and MgO-Fe₃O₄-zeolite (e), TEM image of MgO-Fe₃O₄-zeolite (f). Note. FE-SEM: Field emission scanning electron microscopy; MgO: Magnesium oxide iron oxide; Fe₃O₄: Iron oxide; TEM: Transmission electron microscopy

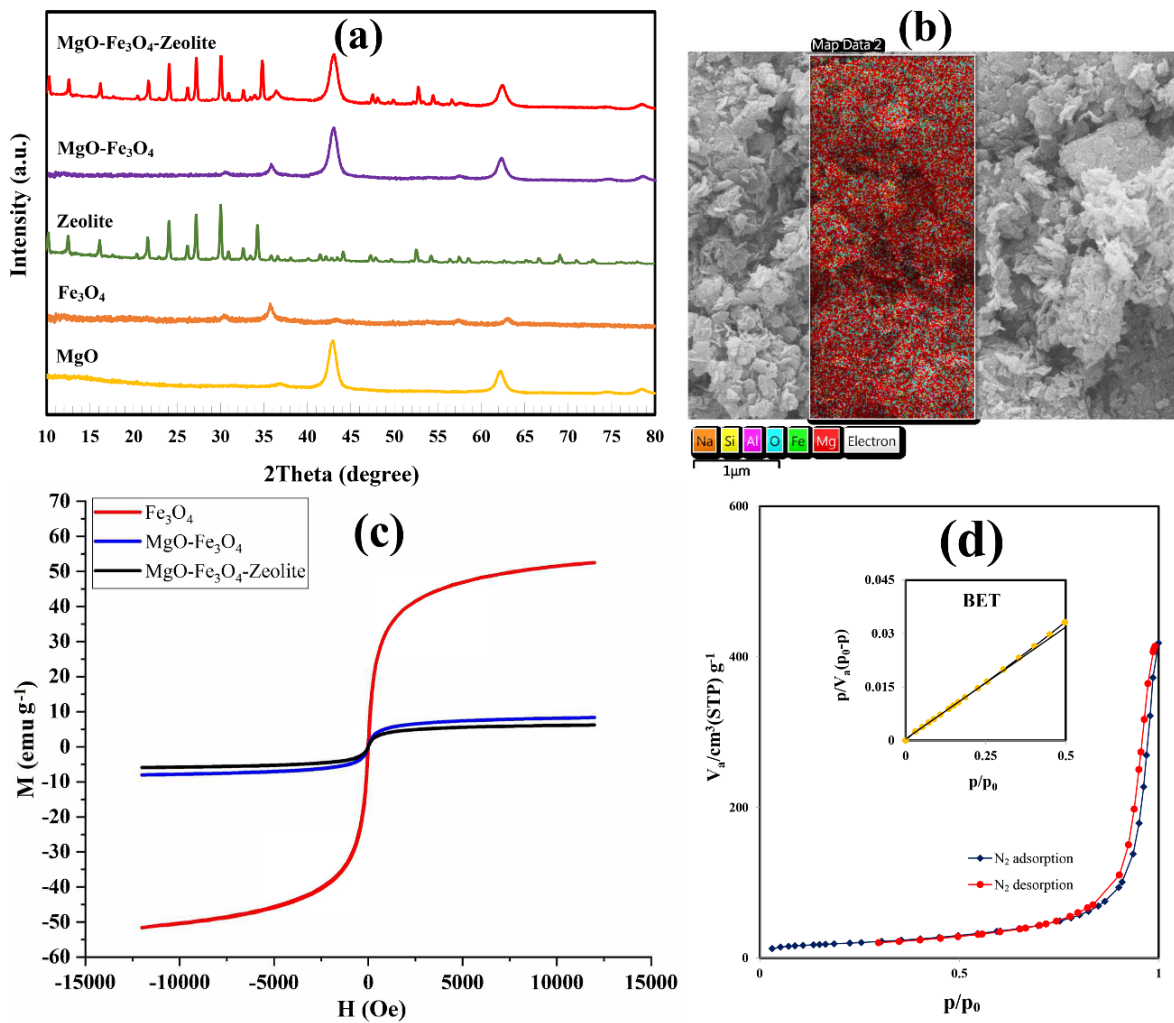


Figure 2. XRD patterns (a), Elemental mapping (b), VSM analysis (c), and N₂ adsorption-desorption Plot (d) of prepared samples. Note. XRD: X-ray diffraction; VSM: Vibrating sample magnetometer

the appearance of the magnetite XRD pattern represents the formation of extremely fine particles with low crystallinity, which was confirmed by the FE-SEM image (Figure 1b). The XRD pattern of zeolite is in agreement with the peaks of the 4A zeolite index (JCPDS card No. 39-0222) [29]. For MgO-Fe₃O₄, the peaks were obtained through combining the peaks of the MgO and Fe₃O₄ specimens, indicating the formation of MgO-Fe₃O₄. As observed in the MgO-Fe₃O₄-zeolite pattern, all the peaks of the composite components (MgO, Fe₃O₄, and 4A zeolite) were well observed, highlighting the successful synthesis of the ternary composite without any impurity.

The composite's EDX elemental mapping (Figure 2b) exhibits the presence of Mg, O, Fe, Si, Al, and Na elements. The elements were distributed in the composite texture.

The magnetic properties of the prepared powders were studied with VSM (Figure 2c). The hysteresis showed the ferromagnetic behavior of binary and ternary composites with a saturation magnetization (*M_s*) in the range of 6-8 emu g⁻¹, which was lower than the magnetite sample. This might be due to the presence of fewer magnetic magnetite particles within the composites. Based on the obtained data, the *M_s* value of Fe₃O₄ is 52 emu g⁻¹, which is slightly less than the reported bulk value of this compound (≈70 emu g⁻¹) [30]. *M_s* is highly dependent on the particle size and decreases with the reduction in particle size. In this study, the low *M_s* value of Fe₃O₄ could be attributed to the small particle size, large surface-to-volume ratio, spin canting effect on the surface, and incomplete particle crystallization [31,32], which is supported by FE-SEM and XRD analysis (Figures 1b and 2a). On the other hand, the coercivity was reduced after compositing the magnetic phase with two non-magnetic phases (MgO and zeolite), and subsequently, an increase was observed in the coercive force. The coercivity depends on various factors, including the substance microstructure, magnetic anisotropy, grain size, and shape. Placing the particles of non-magnetic phases among the magnetite particles affects their surface anisotropy and the way they interact at the interface among the magnetic particles. As a result, it affects the mechanism of electron spinning and the displacement of magnetic domain walls. These parameters lead to a change in the specimen's coercivity after compositing the magnetic phase with non-magnetic phases.

Considering that surface properties are essential parameters in adsorption processes, the textural features of MgO-Fe₃O₄-zeolite were scrutinized using the N₂ adsorption-desorption isotherm. Figure 2d depicts the volume of adsorbed-desorbed nitrogen by the composite as a relative pressure function (*p/p₀*). As shown, the isotherm has a concave-convex shape with a sharp knee point in the low *p/p₀* that corresponds to the IUPAC type IV notation with the H3 hysteresis loop. This also proves the mesoporous nature of the MgO-Fe₃O₄-zeolite

[33]. Isotherm hysteresis indicates that the geometric shape of the pores is cylindrical, and there is a relatively strong relationship between the specimen surface and the adsorbent [34]. Based on the inset of Figure 2d and the Brunauer-Emmett-Teller method, the specific surface area and the pore volume of the composite were 68.90 m²g⁻¹ and 0.59 cm³g⁻¹, respectively. Additionally, the pore size distribution of the MgO-Fe₃O₄-zeolite was determined by the analysis of adsorption-desorption isotherms using the Barrett-Joyner-Halenda method. The mean size of composite pores regarding adsorption and desorption branches was 12.20 nm and 14.03 nm, respectively, indicating the mesoporous nature of the specimen, which is significant in adsorption processes.

3.2. Preliminary screening of adsorbents

The initial step in the investigation of the adsorption process is to find the equilibrium time and adsorbent capacity. For this purpose, the individual adsorption performance of synthesized powders and their binary and ternary composites were assessed by ultrasound-assisted adsorption. Based on the results, the adsorption rate was high for all the adsorbents at initial times, and the equilibrium was achieved after a short time. It is worth noting that parallel adsorption experiments were conducted under magnetic stirring, and the results revealed that the equilibriums were obtained over longer times (Figure not shown). The hybrid adsorption+ultrasound process could accelerate the mass transfer between the adsorbate and adsorbent, thereby reducing the equilibrium time.

Following the comparison of the COD_r extent at the equilibrium time, MgO-Fe₃O₄-zeolite was selected as a susceptible adsorbent in the adsorption of the dairy effluent with an equilibrium time of 25 minutes and used in further experiments under sonication.

3.3. Preliminary trials of dairy wastewater adsorption onto MgO-Fe₃O₄-zeolite

To find parameters affecting the adsorption process and the range of each parameter, the effects of four critical factors were studied, namely, the initial COD, adsorbent dosage, pH, and contact time on COD_r efficiency. To investigate the impacts of the effluent's initial concentration, the samples with a specific concentration (COD₀: 100, 300, 500, 700, and 900 mg L⁻¹) were prepared by diluting the stock solution. After adding the adsorbent at pH = 7 (natural pH of a dairy effluent), the experiments were followed for 25 minutes. According to Figure 3a, as the initial COD increased, COD_r decreased efficiency. To study the effects of the adsorbent dosage, the experiments were performed using five different amounts of MgO-Fe₃O₄-zeolite (1, 2, 3, 4, and 5 g L⁻¹). Based on data in Figure 3b, the percentage of COD_r increased with the increase in the dosage of the adsorbent. The effect of pH

on the adsorption process is influenced by the adsorbate solution pH and the adsorbent pHpzc, and the pHpzc of MgO-Fe₃O₄-zeolite was primarily measured accordingly. Next, dairy effluent samples with a pH of 3, 5, 7, 9, and 11 were prepared, and the experiments were followed. According to Figure 3c, the extent of COD_r increased with the increase in the solution's pH. The effects of the contact time on the adsorption process also implied that the adsorption efficiency increased over time (Figure 3d).

3.4. Assessment of parameter interaction and optimization of the process by RSM

As mentioned in Section 2, RSM-based CCD was used to design the experiments, investigate the parameter interaction, and achieve optimal conditions. Table 1

presents the domain of the parameters and the designed experiments, along with experimental and predicted results.

After importing the experimental data into the software, a quadratic polynomial equation, Eq. (4), was suggested and assessed by ANOVA (Table 2).

$$COD_r(\%) = 60.47 - 5.73X_1 + 3.74X_2 + 5.55X_3 + 4.88X_4 - 0.14X_1X_2 - 0.28X_1X_3 + 0.15X_1X_4 + 0.97X_2X_3 - 1.54X_2X_4 + 0.96X_3X_4 - 0.75X_1^2 + 0.94X_2^2 - 0.015X_3^2 + 2.02X_4^2$$

(4)

According to the ANOVA results, F (32.69) and P (<0.0001) values indicated the high adequacy of the proposed model. The lack of fit F-value (1.63) implies that the lack of fit is not considerable, and the model

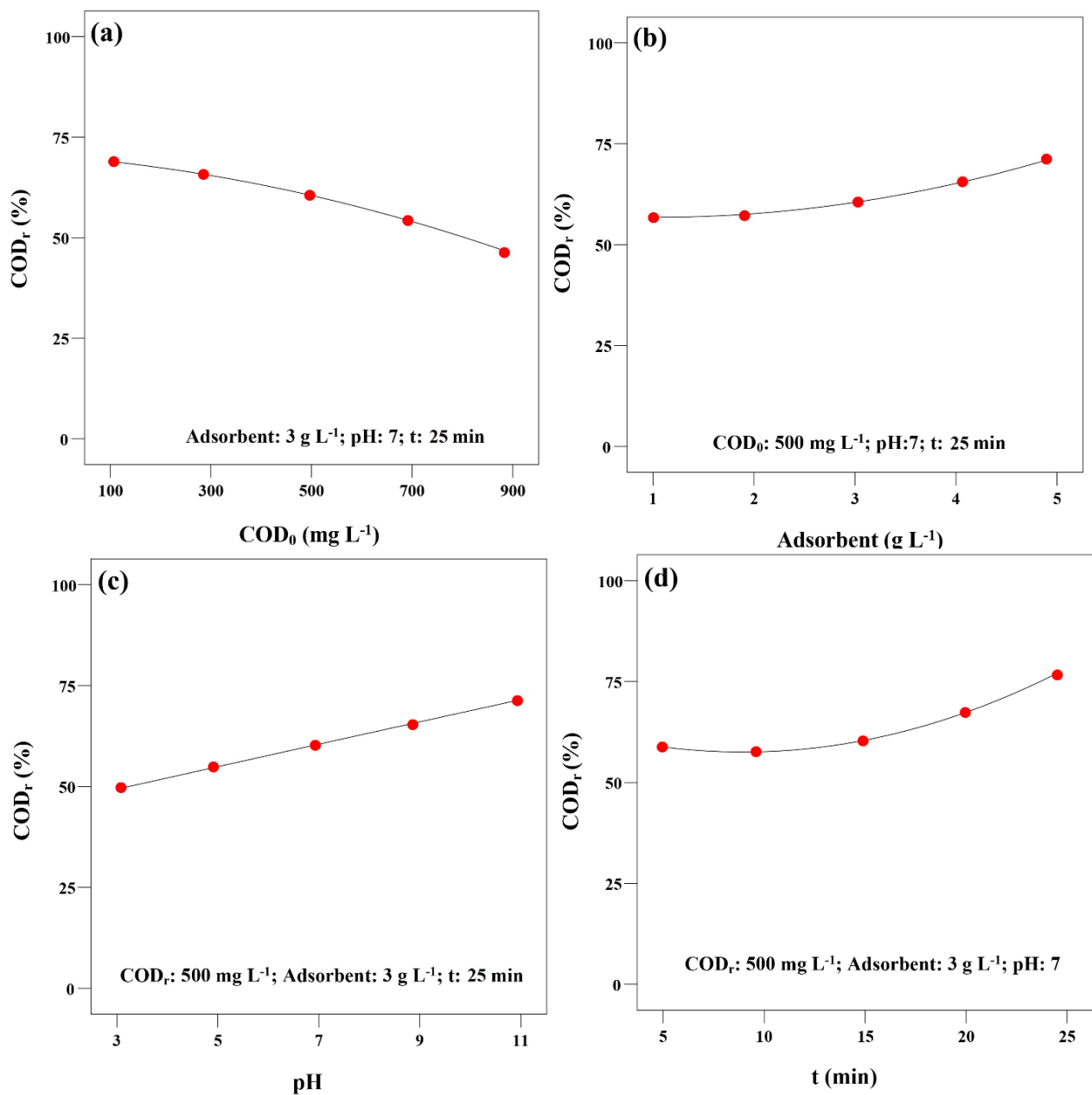


Figure 3. Effect of initial COD (a), adsorbent dosage (b), pH (c), and time (d) on COD_r efficiency. Note. COD: Chemical oxygen demand

covered the data well. Additionally, the correlation coefficient (R^2) value of the model regression was 0.9682, whose appropriate adaption with the adjusted R^2 (0.9387) demonstrated a proper correlation between the experimental and predicted results.

Based on data in Table 2, the “Prob > F” values of X_1X_2 , X_2X_3 , and X_2X_4 were less than 0.0500, and these terms can have a significant effect on COD_r .

The 3D diagrams (response surfaces) of the parameter interaction (X_1X_2 , X_2X_3 , and X_2X_4) were depicted after confirming the accuracy and precision of the selected model.

As shown in Figure 4a, the COD_r efficiency increased with an increase in the adsorbent dosage and a decrease in the initial COD.

Table 2. ANOVA results of the quadratic polynomial model

Source	Sum of squares	DF	Mean square	F-value	P value Prob > F
Model	2649.83	14	189.27	32.69	<0.0001
X_1	787.42	1	787.42	136.01	<0.0001
X_2	335.33	1	335.33	57.92	<0.0001
X_3	739.59	1	739.59	127.75	<0.0001
X_4	571.45	1	571.45	98.70	<0.0001
X_1X_2	0.31	1	0.31	0.054	0.0199
X_1X_3	1.29	1	1.29	0.22	0.6432
X_1X_4	0.38	1	0.38	0.066	0.8009
X_2X_3	15.04	1	15.04	2.60	0.0279
X_2X_4	37.91	1	37.91	6.55	0.0218
X_3X_4	0.15	1	0.15	0.025	0.8758
X_1^2	15.24	1	15.24	2.63	0.1256
X_2^2	24.22	1	24.22	4.18	0.0588
X_3^2	6.431E-003	1	6.431E-003	1.111E-003	0.9739
X_4^2	111.75	1	111.75	19.30	0.0005
Residual	86.84	15	5.79		
Lack of fit	66.47	10	6.65	1.63	0.3071

$R^2=0.9683$ Adjusted $R^2=0.9387$

Note. ANOVA: Analysis of variance; DF: Degree of freedom; R^2 : Coefficient of determination.

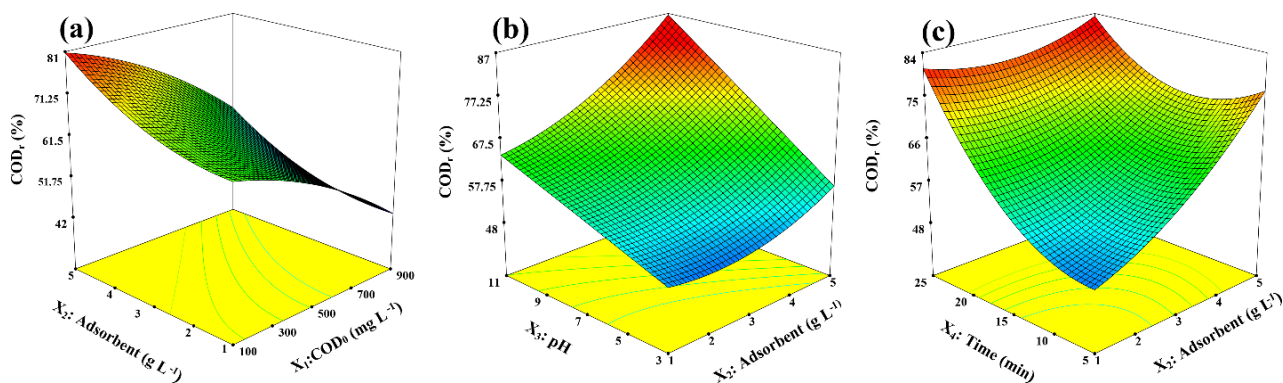


Figure 4. Response Surfaces of Interaction of Adsorption Operating Parameters on COD_r Efficiency. Note. COD: Chemical oxygen demand. The values of the other two parameters in each graph have been considered equal to the central point of their ranges

According to Figures 4b and 4c, the extent of COD_r increased with an increase in the solution’s pH and contact time.

Considering that this experimental design mainly aimed to achieve optimal conditions, the ultrasound-assisted adsorption process was optimized by the software (DX 11), and it was found that under optimal conditions (COD_0 : 300 mgL^{-1} , adsorbent dosage: 4 gL^{-1} , pH: 9, and contact time: 20 minutes), the maximum COD_r efficiency was 83.22%. Performing the experiments under optimal conditions showed that practical efficiency was approximately 80%, with the proximity of experimental and predicted yields re-emphasizing the accuracy and precision of the RSM proposed model.

3.5. Finding the most important parameter affecting the adsorption process by the ANN

The ANN modeling was utilized to select the important operational parameter and reoptimization of the adsorption process. To this end, the values of the experiments designed by RSM, along with experimental COD_r (%) results (Table 1) were entered to the ANN toolbox of Matlab R2020b software as input and output data. Data were processed using the Levenberg-Marquardt back-propagation algorithm [26].

Diverse networks with hidden layer neurons in the range of 2-10 were tested to attain supreme topology based on the least mean square error (MSE) and regression (R) values. Overall, 20 iterations of each topology were performed to resolve errors (Figure not shown). It was found that the epoch 2 had the optimum validation performance with the MSE value of 0.0011, and the structure of the nine neurons of the hidden layer was the best configuration for process modeling.

In addition, the correlation between outputs and targets was evaluated using the regression (R) values of the diagrams illustrated in Figure 5. For all plots, the R -values close to one meant a close relationship between outputs and target values. This is quite clear from the comparison of actual and ANN-predicted results in Table 1.

After model approval, the weight matrix was

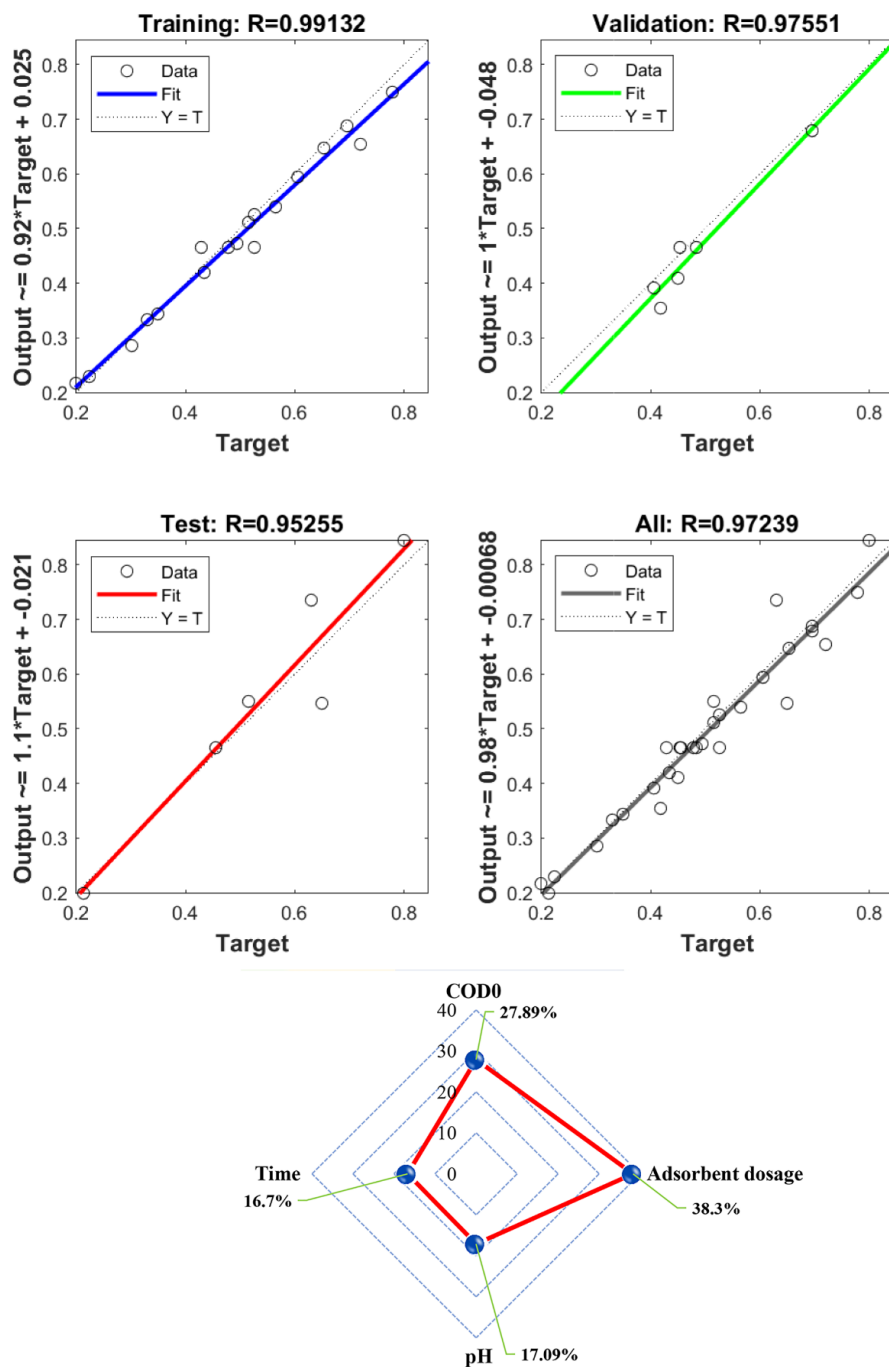


Figure 5. Regression plots for the evaluation of the ANN Model validity, along with relative importance of operational parameters on COD_r (%). Note. ANN: Artificial neural network; COD: Chemical oxygen demand.

acquired, and Garson’s equation [26] based on the connection weights (Table 3) was employed to assess the relative significance of the operating factors on COD_r (%); the results are illustrated as a radar chart in Figure 5. Undoubtedly, the amount of the adsorbent is the vital operational factor with a 38.30% effect on COD_r efficiency.

3.6. Adsorbent stability and reusability assessment

The reusability of the adsorbent should be considered due to economic aspects. For this purpose, the used

adsorbent was collected with a magnet, and it was dried and reused following the desorption process (washing with 0.5 M HNO₃ and DI water). The results of frequent experiments demonstrated that the adsorbent could be reused after multiple times with a slight reduction in efficiency. These findings confirmed the durability and reusability of the adsorbent and implicated the economic aspect of its application.

3.7. Adsorption isotherms

Designing an optimal adsorption system requires a better

Table 3. Weight matrix

Neuron	IW _{ji} [*]				LW _{ji} ^{**}
	X ₁	X ₂	X ₃	X ₄	COD _r (%)
1	1.625	1.437	0.702	-0.445	0.231
2	-0.105	-1.449	1.533	-0.198	0.643
3	0.308	-1.468	0.412	1.808	0.340
4	-0.313	2.004	-1.019	0.228	-0.400
5	-1.415	1.763	0.162	0.035	1.274
6	0.418	0.363	-0.776	-2.246	-0.495
7	0.334	1.491	-1.198	-0.978	0.485
8	-1.760	1.566	-0.434	-0.368	-0.368
9	-2.337	0.783	-0.038	0.688	-0.684

Note. IW: Input weight matrix; LW: Layer weight.

* Weight to the *j*th neuron of the hidden layer from the *i*th input parameter.

** Weight to the output layer from the *j*th neuron of the hidden layer.

understanding of the adsorbent-adsorbate interaction. Adsorption isotherms are equilibrium data used to describe the adsorbent-adsorbate interaction at a constant temperature. Isotherms also indicate the adsorption capacity of an adsorbent.

The isothermal studies of dairy effluent adsorption by MgO-Fe₃O₄-zeolite were conducted by varying the initial COD (100-900 mgL⁻¹) at 25 °C and the optimum specified conditions. The adsorption data were fitted with the Langmuir, Freundlich, Temkin, Redlich-Peterson, and Dubinin-Radushkevich isotherm models; the equations of these models and the values of calculated parameters are summarized in Table 4. The correlation coefficient (*R*²) and chi-squared (χ^2), Eqs. 5 and 6, respectively, were employed to judge the fit of the model with experimental data.

$$R^2 = 1 - \frac{\sum_{i=1}^n (q_{e,exp} - q_{e,cal})^2}{\sum_{i=1}^n (q_{e,exp} - \bar{q}_{e,exp})^2} \quad (5)$$

$$\chi^2 = \sum_{i=1}^n \frac{(q_{e,exp} - q_{e,cal})^2}{q_{e,cal}} \quad (6)$$

where $q_{e,exp}$ and $q_{e,cal}$ are the experimental and calculated equilibrium capacity (mgg⁻¹), respectively. $\bar{q}_{e,exp}$ represents the average of equilibrium adsorption capacity obtained by experimental data.

The Langmuir model describes a homogeneous and monolayer adsorption of the adsorbate with the same energy on the active sites of the adsorbent. The Freundlich model is based on the heterogeneous and multilayer adsorption of the adsorbate over the adsorbent surface. The Temkin model supposes that the adsorption heat resulting from adsorbent-adsorbate chemical interactions decreases linearly with coverage. The model of Redlich-Peterson is applied in both homogeneous and heterogeneous adsorption processes, including the privilege of both Langmuir and Freundlich models. The

Table 4. Isotherm and kinetics parameters along with their regression analysis and error functions

Model	Equation	Parameter
Isotherm Langmuir	$q_e = \frac{q_m K_L C_e}{1 + K_L C_e}$	$q_m = 333.33 \text{ mg g}^{-1}$
		$K_L = 3.28 \times 10^{-3} \text{ L mg}^{-1}$
Freundlich	$q_e = K_F C_e^{\frac{1}{n}}$	$R^2 = 0.930$
		$\chi^2 = 0.051$
		$n = 1.40$
Temkin	$q_e = \frac{RT}{\Delta Q} \ln(K_T C_e)$	$\Delta Q = 54.48 \text{ J mol}^{-1}$
		$K_T = 0.07 \text{ L g}^{-1}$
Redlich-Peterson	$q_e = \frac{AC_e}{1 + BC_e^B}$	$R^2 = 0.991$
		$\chi^2 = 0.017$
		$A = 1.008 \text{ (L mg}^{-1})^B$
Dubinin-Radushkevich	$q_e = q_m \exp(-\beta \varepsilon^2)$	$B = 1 \text{ L mg}^{-1}$
		$g = 0.47$
Kinetics Lagergren's pseudo 1 st order	$q_t = q_e (1 - e^{-k_t t})$	$R^2 = 0.836$
		$\chi^2 = 0.281$
Ho's pseudo 2 nd order	$q_t = \frac{k_2 q_e^2 t}{1 + k_2 q_e t}$	$B = 10^{-4} \text{ mol}^2 \text{ kJ}^{-2}$
		$q_m = 109.07 \text{ mg g}^{-1}$
Elovich	$q_t = \ln(\alpha \beta t)^{\frac{1}{\beta}}$	$R^2 = 0.724$
		$\chi^2 = 0.279$
Intraparticle diffusion	$q_t = k_{id} t^{0.5} + C$	$k_t = 0.15 \text{ min}^{-1}$
		$q_e = 65.77 \text{ mg g}^{-1}$
Ho's pseudo 2 nd order	$q_t = \frac{k_2 q_e^2 t}{1 + k_2 q_e t}$	$R^2 = 0.641$
		$\chi^2 = 0.064$
Elovich	$q_t = \ln(\alpha \beta t)^{\frac{1}{\beta}}$	$k_2 = 9.97 \times 10^{-4} \text{ g mg}^{-1} \text{ min}^{-1}$
		$q_e = 62.34 \text{ mg g}^{-1}$
Intraparticle diffusion	$q_t = k_{id} t^{0.5} + C$	$R^2 = 0.952$
		$\chi^2 = 0.008$
Elovich	$q_t = \ln(\alpha \beta t)^{\frac{1}{\beta}}$	$\alpha = 18.48 \text{ mg g}^{-1} \text{ min}^{-1}$
		$\beta = 0.05 \text{ g mg}^{-1}$
Intraparticle diffusion	$q_t = k_{id} t^{0.5} + C$	$R^2 = 0.945$
		$\chi^2 = 0.012$
Elovich	$q_t = \ln(\alpha \beta t)^{\frac{1}{\beta}}$	$k_{id} = 12.89 \text{ mg g}^{-1} \text{ min}^{-0.5}$
		$C = 0.40 \text{ mg g}^{-1}$
Intraparticle diffusion	$q_t = k_{id} t^{0.5} + C$	$R^2 = 0.971$
		$\chi^2 = 0.971$

Dubinin-Radushkevich model is often used to predict the physical or chemical nature of adsorption where the magnitude of the mean adsorption energy (ε) < 8, ≈ 8-16, or > 20 kJmol⁻¹ indicates the physical adsorption, ion exchange, or chemisorption of the process [35,36].

Polymath software (version 6.10) was employed to draw nonlinear graphs and compute isotherm constants. The results (Figure 6a and Table 4) implied that the Temkin model fitted well with the experimental data (because of the highest *R*² and the lowest χ^2).

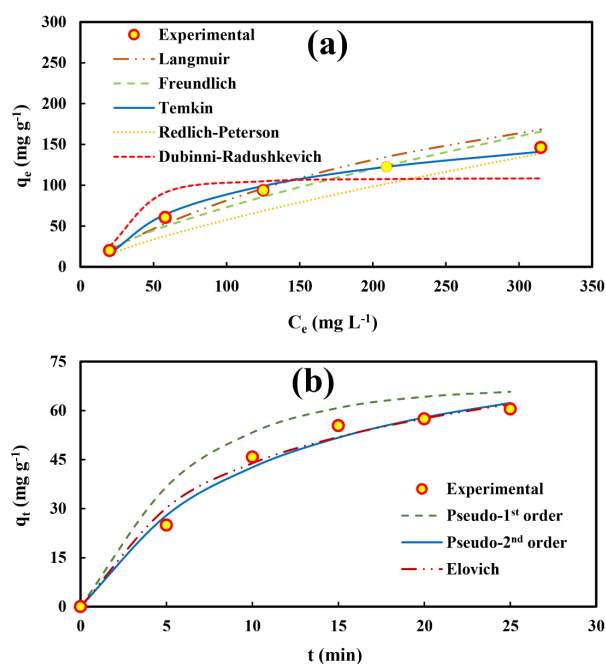


Figure 6. Comparison of adsorption isotherm models (a) and adsorption kinetics models (b) with experimental data

3.8. Adsorption kinetics

One of the most important factors in designing an adsorption system is to predict the adsorption process rate. The adsorption kinetics represents the trend of changes in adsorption capacity over time. The estimation of this trend provides valuable insight for determining the type of the adsorption process mechanism in a given system. Hence, four well-known kinetics models (i.e., the Lagergren's pseudo 1st order, Ho's pseudo 2nd order, Elovich, and intraparticle diffusion models) were adopted to study the adsorption kinetics over a period time of 0-25 minutes under optimal conditions. Table 4 presents the equation of the kinetics models, along with the data extracted from these models.

The 1st order Lagergren model is based on adsorbent capacity and is applicable once the adsorption occurs using a diffusion mechanism through a boundary layer; meanwhile, the 2nd order Ho equation shows that chemical adsorption is a dominant and controlling mechanism in the adsorption process [37,38]. The Elovich model is an appropriate model for describing chemisorption processes and is mainly used in heterogeneous adsorption [39]. The Weber-Morris intraparticle diffusion model is utilized to elucidate the diffusion mechanism of adsorption systems. In this model, the intercept (C) indicates the thickness of the boundary layer, where zero implies that the adsorption process is only controlled by intraparticle diffusion [40].

Similar to the previous stage, Polymath software was employed to draw nonlinear graphs and compute rate constants. According to the obtained results (Figure 6b and Table 4), the adsorption kinetics could be better fitted by the pseudo 2nd order and Elovich models.

The comparison of the q_e calculated from the Ho's model (62.34 mgg⁻¹) with experimental q_e (60.48 mgg⁻¹) revealed a good correlation between them. Furthermore, the value of k_2q_e ($6.62 \times 10^{-2} \text{ min}^{-1}$) indicated that adsorption onto the ternary composite of MgO-Fe₃O₄-zeolite was a swift process. In addition, the non-zero value of the intercept in the intraparticle diffusion model ($C = 0.4 \text{ mgg}^{-1}$) showed that this model was not the only rate-controlling stage, and the adsorption of dairy effluent by MgO-Fe₃O₄-zeolite followed the pseudo 2nd order + Elovich + intraparticle diffusion kinetics models.

3.9. Adsorption thermodynamics

To evaluate the thermodynamics of the process, the adsorption of the dairy effluent onto MgO-Fe₃O₄-zeolite was studied under optimal conditions at three different temperatures. The results demonstrated that COD_r efficiency increased with an increase in the temperature. Thermodynamics parameters (ΔG° , ΔH° , and ΔS°) were computed using Eqs. (7) and (8):

$$\Delta G^\circ = -RT \ln K_C \quad (K_C = \frac{q_e}{C_e}) \quad (7)$$

$$\ln K_C = -\frac{\Delta H^\circ}{R} \left(\frac{1}{T}\right) + \frac{\Delta S^\circ}{R} \quad (8)$$

where K_C , q_e (mgg⁻¹), and C_e (mgL⁻¹) are the equilibrium constant, equilibrium adsorption capacity, and equilibrium COD extent at different temperatures, respectively [41].

Taking into account Eq. (7) and substituting equilibrium constants at 298, 308, and 318 K, the ΔG° values of -101.90, -514.02, and -939.58 Jmol⁻¹ were obtained, implying that the process was spontaneous.

Considering Eq. (8) and plotting the $\ln K_C$ vs. $1/T$ (Figure not shown), the values of ΔH° (12.37 kJmol⁻¹) and ΔS° (41.89 JK⁻¹mol⁻¹) were achieved from the slope and intercept, respectively.

4. Discussion

The FE-SEM and TEM images (Figure 1) confirmed the composite formation through the distribution of MgO and Fe₃O₄ spherical nanoparticles on 4A zeolite cubic particles. The XRD patterns of MgO, Fe₃O₄, and 4A zeolite (Figure 2a) appeared at their respective diffraction angles, highlighting the success of their preparation. For MgO-Fe₃O₄-zeolite, characteristic diffraction peaks corresponding to MgO, Fe₃O₄, and 4A zeolite justified the creation of the ternary composite without impurities. The EDX-elemental mapping analysis (Figure 2b) confirmed the presence of Mg, O, Fe, Si, Al, and Na elements in the composite texture. Moreover, the VSM analysis (Figure 2c) demonstrated the ferromagnetic behavior of the ternary composite. The N₂ adsorption-desorption results (Figure 2d) corroborated the construction of the composite with a mesoporous structure.

The experiments to find the equilibrium time revealed that the equilibrium was achieved after a short time. In the adsorption process by MgO and Fe₃O₄, the most significant changes occurred during the first 5 minutes, after which the COD_r efficiency remained almost constant. The results also demonstrated that the adsorption onto MgO-Fe₃O₄ and MgO-Fe₃O₄-zeolite was impressive in the first 25 minutes. The number of active sites in the adsorbent was extremely high in the initial stages, but the adsorption sites became saturated over time, and the adsorption rate was controlled by transferring from external to internal sites [42]. Based on the results, there was a substantial difference in COD_r efficiency by individual adsorbents compared with their binary and ternary composites. A low COD_r extent by single adsorbents could be ascribed to limited surface sites, the high hydrophilicity of MgO, and the agglomeration possibility of Fe₃O₄ nanoparticles in aqueous solutions [19,43].

The RSM-based CCD was applied to design the adsorption experiments. The response surfaces of the parameter interaction were illustrated after confirming the accuracy and precision of the selected model (Figure 4). Increasing the amount of the adsorbent increased the number of adsorption sites, thereby augmenting the number of adsorbed micropollutant molecules. On the other hand, as the initial COD of the dairy effluent increased, the competition for accessing the active sites increased, and the entire adsorbent surface was exposed to contaminant molecules. Moreover, the electrostatic repulsion between the adsorbed and soluble micropollutants led to a COD_r reduction at high concentrations [44,45]. Other researchers reported similar results for the adsorption of organics in dairy wastewater on modified nano-montmorillonite [6]. The leading reason for increased efficiency by the increment in the solution pH and adsorbent dosage was electrostatic interactions between micropollutant molecules and the surface of the MgO-Fe₃O₄-zeolite. In fact, the dairy effluent pH is almost neutral or slightly alkaline, but it may become relatively acidic given the presence of lactic acid generated by lactose [1-3,46,47]. Accordingly, the deprotonation of dairy effluent compounds is possible in alkaline media. Therefore, a strong electrostatic attraction could be expected between the positive surface of the adsorbent (pHpzc=11) and the deprotonated organic species by the increase in the solution pH. The increase in COD_r over time represents the fact that the probability of the adsorbent-adsorbate contact increases over a longer duration, finally reaching its maximum value at equilibrium.

Based on the ANN modeling results, the relative significance of the operating factors was as adsorbent dosage > initial COD > pH > sonication time.

The adsorption of dairy wastewater by the composite was consistent with the Temkin isotherm model. It could

be speculated that the adsorption of dairy wastewater by MgO-Fe₃O₄-zeolite was mainly due to chemical interactions. The positive value of ΔQ indicates that the adsorption of the dairy effluent by MgO-Fe₃O₄-zeolite is an endothermic process supported by thermodynamics results (ΔH° > 0).

The kinetics data were well described by both Ho's pseudo 2nd order and Elovich models. Hence, the adsorption of the dairy effluent onto MgO-Fe₃O₄-zeolite was most probably due to chemisorption, which is supported by isothermal results.

Increasing COD_r efficiency with the increase in the temperature could be attributed to the increase in the kinetic energy of micropollutant molecules with the rise in temperature, as well as the increase in their collisions with the adsorbent surface [48].

Given the positive values of enthalpy and entropy, the process was endothermic with an increase in disorder at the adsorbent-adsorbate interface.

To further evaluate the adsorption capacity of the adsorbent prepared in this study, the adsorption capacities of MgO-Fe₃O₄-zeolite and other adsorbents prepared in the literature to dairy wastewater are listed in Table 5 [49-54]. Based on the data, MgO-Fe₃O₄-zeolite exhibits excellent adsorption performance and has great competitiveness in this research field, indicating that it is a potential adsorbent for dairy wastewater treatment. In addition, MgO-Fe₃O₄-zeolite has magnetic behavior and thus has the advantage of being recyclable.

4.1. Possible adsorption mechanism

Generally, various factors are involved in the accosting of the adsorbate to the adsorbent surface, including physical, chemical, and electrostatic interactions. According to the aforementioned results, the coulomb's attractive forces, along with chemical adsorption were the main reasons for dairy effluent adsorption by MgO-Fe₃O₄-zeolite. Given that the obtained pHpzc for the composite was 11, the composite surface had a negative and positive electric charge at pH > 11 and pH < 11, respectively. Most compounds in dairy effluents are organics. It is more likely that they are deprotonated in alkaline

Table 5. Comparison of different adsorbents for the adsorption of dairy wastewater

Adsorbent	Contact time	COD _r (%)	Reference
Copper oxide nanoparticles	120 min	77	[49]
Carbon nanotubes	15 h	50	[50]
Modified dried activated sludge	120 min	80	[51]
Soil	9 h	46	[52]
Graphene oxide	30 min	80	[53]
Chitosan	240 min	90	[54]
MgO-Fe ₃ O ₄ -zeolite	20 min	83	This study

Note. COD: Chemical oxygen demand; Magnesium oxide iron oxide; Fe₃O₄: Iron oxide.

media [46,47]. Accordingly, it could be expected that by increasing the pH of the solution, a strong electrostatic attraction occurs between the adsorbent positive surface and deprotonated organic species. On the other hand, the nature of the chemisorption of the process was also partially revealed by the results obtained from isothermal and kinetics studies. In this regard, the role of hydrogen bonding and Van der Waals interactions must be taken into consideration [55,56].

5. Conclusion

In the current research, the MgO-Fe₃O₄-zeolite nanocomposite was prepared as a novel adsorbent for adsorbing the organic compounds of the dairy effluent by ultrasound-assisted adsorption. It was concluded that the synergistic effects of MgO, Fe₃O₄, and zeolite could facilitate the adsorption of organics in the effluent and increase the efficiency of the adsorption process. The CCD based on RSM was exploited in the planning stage of the experimental approach, and it was found that the maximum COD_r efficiency was 83.22% under optimal conditions. The evaluation of the adsorption isotherm and kinetics represented that the process was well fitted by the Temkin isotherm model and Ho's 2nd order kinetics model, indicating that the process belonged to chemisorption. The thermodynamics studies showed that the adsorption of the dairy effluent by the magnetic nanocomposite was endothermic ($\Delta H^\circ > 0$) and spontaneous ($\Delta G^\circ < 0$).

The significant results of this work emphasize the applicability of the prepared magnetically recyclable adsorbent toward sequestering different micropollutants in practical engineering.

Acknowledgments

The author would like to thank Tabriz Branch, Islamic Azad University for providing facilities and technical support.

Conflict of Interests

The author declares that he has no known competing financial interests or personal relationships that could have appeared to influence the work reported in this paper.

References

1. Amini M, Younesi H, Zinatizadeh Lorestani AA, Najafpour G. Determination of optimum conditions for dairy wastewater treatment in UAASB reactor for removal of nutrients. *Bioresour Technol.* 2013;145:71-9. doi: [10.1016/j.biortech.2013.01.111](https://doi.org/10.1016/j.biortech.2013.01.111).
2. Daneshvar E, Zarrinmehr MJ, Koutra E, Kornaros M, Farhadian O, Bhatnagar A. Sequential cultivation of microalgae in raw and recycled dairy wastewater: microalgal growth, wastewater treatment and biochemical composition. *Bioresour Technol.* 2019;273:556-64. doi: [10.1016/j.biortech.2018.11.059](https://doi.org/10.1016/j.biortech.2018.11.059).
3. Muniz GL, Silva T, Borges AC. Assessment and optimization of the use of a novel natural coagulant (*Guazuma ulmifolia*) for dairy wastewater treatment. *Sci Total Environ.* 2020;744:140864. doi: [10.1016/j.scitotenv.2020.140864](https://doi.org/10.1016/j.scitotenv.2020.140864).
4. Li Z, Zhang Y, Cao Y, Zhou S, Han Y, Yue L. Characterization of Sn-MOF and its adsorption application for Acid Red 3R. *Mater Lett.* 2021;282:128647. doi: [10.1016/j.matlet.2020.128647](https://doi.org/10.1016/j.matlet.2020.128647).
5. Liu WB, Cui GN, Wang H, Zhang DM, Wu RX, Li L, et al. Efficient and selective adsorption of dye in aqueous environment employing a functional Zn(II)-based metal organic framework. *J Solid State Chem.* 2020;292:121740. doi: [10.1016/j.jssc.2020.121740](https://doi.org/10.1016/j.jssc.2020.121740).
6. Zhang W, Zhang L, Jiang X, Liu X, Li Y, Zhang Y. Enhanced adsorption removal of aflatoxin B1, zearalenone and deoxynivalenol from dairy cow rumen fluid by modified nano-montmorillonite and evaluation of its mechanism. *Anim Feed Sci Technol.* 2020;259:114366. doi: [10.1016/j.anifeedsci.2019.114366](https://doi.org/10.1016/j.anifeedsci.2019.114366).
7. Hong M, Yu L, Wang Y, Zhang J, Chen Z, Dong L, et al. Heavy metal adsorption with zeolites: the role of hierarchical pore architecture. *Chem Eng J.* 2019;359:363-72. doi: [10.1016/j.cej.2018.11.087](https://doi.org/10.1016/j.cej.2018.11.087).
8. Piri F, Mollahosseini A, khadir A, Milani Hosseini M. Enhanced adsorption of dyes on microwave-assisted synthesized magnetic zeolite-hydroxyapatite nanocomposite. *J Environ Chem Eng.* 2019;7(5):103338. doi: [10.1016/j.jece.2019.103338](https://doi.org/10.1016/j.jece.2019.103338).
9. Jiang N, Shang R, Heijman SGJ, Rietveld LC. Adsorption of triclosan, trichlorophenol and phenol by high-silica zeolites: adsorption efficiencies and mechanisms. *Sep Purif Technol.* 2020;235:116152. doi: [10.1016/j.seppur.2019.116152](https://doi.org/10.1016/j.seppur.2019.116152).
10. Mohamed RM, Shawky A, Mkhallid IA. Facile synthesis of MgO and Ni-MgO nanostructures with enhanced adsorption of methyl blue dye. *J Phys Chem Solids.* 2017;101:50-7. doi: [10.1016/j.jpcs.2016.10.009](https://doi.org/10.1016/j.jpcs.2016.10.009).
11. Cui W, Li P, Wang Z, Zheng S, Zhang Y. Adsorption study of selenium ions from aqueous solutions using MgO nanosheets synthesized by ultrasonic method. *J Hazard Mater.* 2018;341:268-76. doi: [10.1016/j.jhazmat.2017.07.073](https://doi.org/10.1016/j.jhazmat.2017.07.073).
12. Zheng X, Zhou Y, Liu X, Fu X, Peng H, Lv S. Enhanced adsorption capacity of MgO/N-doped active carbon derived from sugarcane bagasse. *Bioresour Technol.* 2020;297:122413. doi: [10.1016/j.biortech.2019.122413](https://doi.org/10.1016/j.biortech.2019.122413).
13. Bekhti H, Bouchafaa H, Melouki R, Travert A, Boucheffa Y. Adsorption of CO₂ over MgO-impregnated NaYzeolites and modeling study. *Microporous Mesoporous Mater.* 2020;294:109866. doi: [10.1016/j.micromeso.2019.109866](https://doi.org/10.1016/j.micromeso.2019.109866).
14. Guoj. Adsorption characteristics and mechanisms of high-levels of ammonium from swine wastewater using natural and MgO modified zeolites. *Desalin Water Treat.* 2016;57(12):5452-63. doi: [10.1080/19443994.2014.1003334](https://doi.org/10.1080/19443994.2014.1003334).
15. Gao F, Wang S, Chen G, Duan J, Dong J, Wang W. A facile approach to the fabrication of MgO@Y composite for CO₂ capture. *Adsorption.* 2020;26(5):701-9. doi: [10.1007/s10450-019-00147-w](https://doi.org/10.1007/s10450-019-00147-w).
16. Sivashankar R, Sathya AB, Vasantharaj K, Sivasubramanian V. Magnetic composite an environmental super adsorbent for dye sequestration—a review. *Environ Nanotechnol Monit Manag.* 2014;1-2:36-49. doi: [10.1016/j.enmm.2014.06.001](https://doi.org/10.1016/j.enmm.2014.06.001).
17. Kefeni KK, Mamba BB, Msagati TAM. Application of spinel ferrite nanoparticles in water and wastewater treatment: a review. *Sep Purif Technol.* 2017;188:399-422. doi: [10.1016/j.seppur.2017.07.015](https://doi.org/10.1016/j.seppur.2017.07.015).
18. Salem ANM, Ahmed MA, El-Shahat MF. Selective adsorption of amaranth dye on Fe₃O₄/MgO nanoparticles. *J Mol Liq.* 2016;219:780-8. doi: [10.1016/j.molliq.2016.03.084](https://doi.org/10.1016/j.molliq.2016.03.084).
19. Liu X, Tian J, Li Y, Sun N, Mi S, Xie Y, et al. Enhanced dyes adsorption from wastewater via Fe₃O₄ nanoparticles functionalized activated carbon. *J Hazard Mater.* 2019;373:397-407. doi: [10.1016/j.jhazmat.2019.03.103](https://doi.org/10.1016/j.jhazmat.2019.03.103).
20. Zhao L, Lv W, Hou J, Li Y, Duan J, Ai S. Synthesis of magnetically

- recyclable g-C₃N₄/Fe₃O₄/ZIF-8 nanocomposites for excellent adsorption of malachite green. *Microchem J.* 2020;152:104425. doi: [10.1016/j.microc.2019.104425](https://doi.org/10.1016/j.microc.2019.104425).
21. Baziari M, Azari A, Karimaei M, Gupta VK, Agarwal S, Sharafi K, et al. MWCNT-Fe₃O₄ as a superior adsorbent for microcystins LR removal: investigation on the magnetic adsorption separation, artificial neural network modeling, and genetic algorithm optimization. *J Mol Liq.* 2017;241:102-13. doi: [10.1016/j.molliq.2017.06.014](https://doi.org/10.1016/j.molliq.2017.06.014).
 22. Dashamiri S, Ghaedi M, Dashtian K, Rahimi MR, Goudarzi A, Jannesar R. Ultrasonic enhancement of the simultaneous removal of quaternary toxic organic dyes by CuO nanoparticles loaded on activated carbon: central composite design, kinetic and isotherm study. *Ultrason Sonochem.* 2016;31:546-57. doi: [10.1016/j.ultsonch.2016.02.008](https://doi.org/10.1016/j.ultsonch.2016.02.008).
 23. Rajput S, Pittman CU Jr, Mohan D. Magnetic magnetite (Fe₃O₄) nanoparticle synthesis and applications for lead (Pb²⁺) and chromium (Cr⁶⁺) removal from water. *J Colloid Interface Sci.* 2016;468:334-46. doi: [10.1016/j.jcis.2015.12.008](https://doi.org/10.1016/j.jcis.2015.12.008).
 24. Mahmoudi E, Behnajady MA. Synthesis of Fe₃O₄@NiO core-shell nanocomposite by the precipitation method and investigation of Cr(VI) adsorption efficiency. *Colloids Surf A Physicochem Eng Asp.* 2018;538:287-96. doi: [10.1016/j.colsurfa.2017.11.020](https://doi.org/10.1016/j.colsurfa.2017.11.020).
 25. Ataei A, Mehrizad A, Zare K. Photocatalytic degradation of cefazoline antibiotic using zeolite-supported CdS/CaFe₂O₄ Z-scheme photocatalyst: optimization and modeling of process by RSM and ANN. *J Mol Liq.* 2021;328:115476. doi: [10.1016/j.molliq.2021.115476](https://doi.org/10.1016/j.molliq.2021.115476).
 26. Attarikhsharaghi N, Zare K, Mehrizad A, Modirshahla N, Behnajady MA. Zeolite 4A supported CdS/g-C₃N₄ type-II heterojunction: a novel visible-light-active ternary nanocomposite for potential photocatalytic degradation of cefoperazone. *J Mol Liq.* 2021;342:117479. doi: [10.1016/j.molliq.2021.117479](https://doi.org/10.1016/j.molliq.2021.117479).
 27. Wang B, Xiong X, Ren H, Huang Z. Preparation of MgO nanocrystals and catalytic mechanism on phenol ozonation. *RSC Adv.* 2017;7(69):43464-73. doi: [10.1039/c7ra07553g](https://doi.org/10.1039/c7ra07553g).
 28. Mahdavi M, Bin Ahmad M, Haron MJ, Gharayebi Y, Shameli K, Nadi B. Fabrication and characterization of SiO₂/(3-aminopropyl) triethoxysilane-coated magnetite nanoparticles for lead (II) removal from aqueous solution. *J Inorg Organomet Polym Mater.* 2013;23(3):599-607. doi: [10.1007/s10904-013-9820-2](https://doi.org/10.1007/s10904-013-9820-2).
 29. Koh PY, Yan J, Teja A. Precipitation and growth of magnesium hydroxide nanopetals on zeolite 4A surfaces. *J Cryst Growth.* 2011;331(1):56-63. doi: [10.1016/j.jcrysgro.2011.07.006](https://doi.org/10.1016/j.jcrysgro.2011.07.006).
 30. Roca AG, Marco JF, del Puerto Morales M, Serna CJ. Effect of nature and particle size on properties of uniform magnetite and maghemite nanoparticles. *J Phys Chem C.* 2007;111(50):18577-84. doi: [10.1021/jp075133m](https://doi.org/10.1021/jp075133m).
 31. Wang T, Zhang L, Wang H, Yang W, Fu Y, Zhou W, et al. Controllable synthesis of hierarchical porous Fe₃O₄ particles mediated by poly(diallyldimethylammonium chloride) and their application in arsenic removal. *ACS Appl Mater Interfaces.* 2013;5(23):12449-59. doi: [10.1021/am403533v](https://doi.org/10.1021/am403533v).
 32. Petcharoen K, Sirivat A. Synthesis and characterization of magnetite nanoparticles via the chemical co-precipitation method. *Mater Sci Eng B.* 2012;177(5):421-7. doi: [10.1016/j.mseb.2012.01.003](https://doi.org/10.1016/j.mseb.2012.01.003).
 33. Rouquerol J, Rouquerol F, Llewellyn P, Maurin G, Sing KS. *Adsorption by Powders and Porous Solids: Principles, Methodology and Applications.* Academic Press; 2013. doi: [10.1016/b978-0-12-598920-6.x5000-3](https://doi.org/10.1016/b978-0-12-598920-6.x5000-3).
 34. Thommes M, Kaneko K, Neimark AV, Olivier JP, Rodriguez-Reinoso F, Rouquerol J, et al. Physisorption of gases, with special reference to the evaluation of surface area and pore size distribution (IUPAC Technical Report). *Pure Appl Chem.* 2015;87(9-10):1051-69. doi: [10.1515/pac-2014-1117](https://doi.org/10.1515/pac-2014-1117).
 35. Gimbert F, Morin-Crini N, Renault F, Badot PM, Crini G. Adsorption isotherm models for dye removal by cationized starch-based material in a single component system: error analysis. *J Hazard Mater.* 2008;157(1):34-46. doi: [10.1016/j.jhazmat.2007.12.072](https://doi.org/10.1016/j.jhazmat.2007.12.072).
 36. Azari A, Mahmoudian MH, Hazrati Niari M, Eş I, Dehganifard E, Kiani A, et al. Rapid and efficient ultrasonic assisted adsorption of diethyl phthalate onto FeIIIFe₂IIIIO₄@GO: ANN-GA and RSM-DF modeling, isotherm, kinetic and mechanism study. *Microchem J.* 2019;150:104144. doi: [10.1016/j.microc.2019.104144](https://doi.org/10.1016/j.microc.2019.104144).
 37. Yin L, Lin Y, Jia L. Graphene oxide functionalized magnetic nanoparticles as adsorbents for removal of phthalate esters. *Microchim Acta.* 2014;181(9):957-65. doi: [10.1007/s00604-014-1187-8](https://doi.org/10.1007/s00604-014-1187-8).
 38. Ho YS, McKay G. Pseudo-second order model for sorption processes. *Process Biochem.* 1999;34(5):451-65. doi: [10.1016/s0032-9592\(98\)00112-5](https://doi.org/10.1016/s0032-9592(98)00112-5).
 39. Xiao G, Wang Y, Xu S, Li P, Yang C, Jin Y, et al. Superior adsorption performance of graphitic carbon nitride nanosheets for both cationic and anionic heavy metals from wastewater. *Chin J Chem Eng.* 2019;27(2):305-13. doi: [10.1016/j.cjche.2018.09.028](https://doi.org/10.1016/j.cjche.2018.09.028).
 40. Hasanzadeh V, Rahmanian O, Heidari M. Cefixime adsorption onto activated carbon prepared by dry thermochemical activation of date fruit residues. *Microchem J.* 2020;152:104261. doi: [10.1016/j.microc.2019.104261](https://doi.org/10.1016/j.microc.2019.104261).
 41. Mehrizad A. Adsorption studies of some phenol derivatives onto Ag-cuttlebone nanobiocomposite: modeling of process by response surface methodology. *Res Chem Intermed.* 2017;43(7):4295-310. doi: [10.1007/s11164-017-2874-y](https://doi.org/10.1007/s11164-017-2874-y).
 42. Mehrizad A, Gharbani P. Decontamination of 4-chloro-2-nitrophenol from aqueous solution by graphene adsorption: equilibrium, kinetic, and thermodynamic studies. *Pol J Environ Stud.* 2014;23(6):2111-6. doi: [10.15244/pjoes/26779](https://doi.org/10.15244/pjoes/26779).
 43. Priyadarshini B, Patra T, Sahoo TR. An efficient and comparative adsorption of Congo red and Trypan blue dyes on MgO nanoparticles: kinetics, thermodynamics and isotherm studies. *J Magnes Alloy.* 2021;9(2):478-88. doi: [10.1016/j.jma.2020.09.004](https://doi.org/10.1016/j.jma.2020.09.004).
 44. Chowdhury S, Mishra R, Saha P, Kushwaha P. Adsorption thermodynamics, kinetics and isosteric heat of adsorption of malachite green onto chemically modified rice husk. *Desalination.* 2011;265(1):159-68. doi: [10.1016/j.desal.2010.07.047](https://doi.org/10.1016/j.desal.2010.07.047).
 45. Behnajady MA, Yavari S, Modirshahla N. Investigation on adsorption capacity of TiO₂-P25 nanoparticles in the removal of a mono-azo dye from aqueous solution: a comprehensive isotherm analysis. *Chem Ind Chem Eng Q.* 2014;20(1):97-107. doi: [10.2298/ciceq120610105b](https://doi.org/10.2298/ciceq120610105b).
 46. Dela Justina M, Rodrigues Bagnolin Muniz B, Mattge Bröring M, Costa VJ, Skoronski E. Using vegetable tannin and polyaluminium chloride as coagulants for dairy wastewater treatment: a comparative study. *J Water Process Eng.* 2018;25:173-81. doi: [10.1016/j.jwpe.2018.08.001](https://doi.org/10.1016/j.jwpe.2018.08.001).
 47. Murcia JJ, Hernández-Laverde M, Rojas H, Muñoz E, Navío JA, Hidalgo MC. Study of the effectiveness of the flocculation-photocatalysis in the treatment of wastewater coming from dairy industries. *J Photochem Photobiol A Chem.* 2018;358:256-64. doi: [10.1016/j.jphotochem.2018.03.034](https://doi.org/10.1016/j.jphotochem.2018.03.034).
 48. Mehrizad A, Zare K, Aghaie H, Dastmalchi S. Removal of 4-chloro-2-nitrophenol occurring in drug and pesticide waste by adsorption onto nano-titanium dioxide. *Int J Environ Sci*

- Technol. 2012;9(2):355-60. doi: [10.1007/s13762-012-0038-6](https://doi.org/10.1007/s13762-012-0038-6).
49. Al-Ananzeh NM. Treatment of wastewater from a dairy plant by adsorption using synthesized copper oxide nanoparticles: kinetics and isotherms modeling optimization. *Water Sci Technol.* 2021;83(7):1591-604. doi: [10.2166/wst.2021.089](https://doi.org/10.2166/wst.2021.089).
50. Moradi O, Maleki MS. Removal of COD from dairy wastewater by MWCNTs: adsorption isotherm modeling. *Fuller Nanotub Carbon Nanostructures.* 2013;21(10):836-48. doi: [10.1080/1536383x.2011.613547](https://doi.org/10.1080/1536383x.2011.613547).
51. Bazrafshan E, Kord Mostafapour F, Alizadeh M, Farzadkia M. Dairy wastewater treatment by chemical coagulation and adsorption on modified dried activated sludge: a pilot-plant study. *Desalin Water Treat.* 2016;57(18):8183-93. doi: [10.1080/19443994.2015.1018331](https://doi.org/10.1080/19443994.2015.1018331).
52. Al-Jabari M, Iqefan N, Zahdeh N, Dweik H. Adsorption of organic pollutants from dairy wastewater on soil: pollution problem and control. *Int J Glob Environ Issues.* 2017;16(1-3):149-61. doi: [10.1504/ijgenvi.2017.083425](https://doi.org/10.1504/ijgenvi.2017.083425).
53. Falahati F, Baghdadi M, Aminzadeh B. Treatment of dairy wastewater by graphene oxide nano-adsorbent and sludge separation, using In Situ Sludge Magnetic Impregnation (ISSMI). *Pollution.* 2018;4(1):29-41. doi: [10.22059/poll.2017.233196.276](https://doi.org/10.22059/poll.2017.233196.276).
54. Eulmi A, Hazourli S, Abrane R, Bendaia M, Aitbara A, Touahria S, et al. Evaluation of electrocoagulation and activated carbon adsorption techniques used separately or coupled to treat wastewater from industrial dairy. *Int J Chem React Eng.* 2019;17(12):20180229. doi: [10.1515/ijcre-2018-0229](https://doi.org/10.1515/ijcre-2018-0229).
55. Catherine HN, Ou MH, Manu B, Shih YH. Adsorption mechanism of emerging and conventional phenolic compounds on graphene oxide nanoflakes in water. *Sci Total Environ.* 2018;635:629-38. doi: [10.1016/j.scitotenv.2018.03.389](https://doi.org/10.1016/j.scitotenv.2018.03.389).
56. Suo F, You X, Ma Y, Li Y. Rapid removal of triazine pesticides by P doped biochar and the adsorption mechanism. *Chemosphere.* 2019;235:918-25. doi: [10.1016/j.chemosphere.2019.06.158](https://doi.org/10.1016/j.chemosphere.2019.06.158)

© 2022 The Author(s); This is an open-access article distributed under the terms of the Creative Commons Attribution License (<https://creativecommons.org/licenses/by/4.0/>), which permits unrestricted use, distribution, and reproduction in any medium, provided the original work is properly cited.